*Journal of Advanced Ceramics*
2023, **12**(1): 122–131
https://doi.org/10.26599/JAC.2023.9220671
ISSN 2226-4108
CN 10-1154/TQ

**Research Article**

# Design strategy of phase and microstructure of $Si_3N_4$ ceramics with simultaneously high hardness and toughness

Shao-Jun TANG[a], Wei-Ming GUO[a,*], Shi-Kuan SUN[b], Hua-Tay LIN[a,*]

[a]*School of Electromechanical Engineering, Guangdong University of Technology, Guangzhou 510006, China*
[b]*School of Material Science and Energy Engineering, Foshan University, Foshan 528000, China*

Received: July 11, 2022; Revised: September 30, 2022; Accepted: October 1, 2022


**Abstract:** Aiming to achieve silicon nitride ($Si_3N_4$) ceramics with high hardness and high toughness, the relationships among phase composition, microstructure, and mechanical properties of $Si_3N_4$ ceramics prepared by spark plasma sintering (SPS) at temperatures ranging from 1500 to 1800 ℃ were investigated in this study. Two stages with different phase and microstructure features were observed and summarized. The α–β phase transformation occurs first, and the development and growth of grains lag behind. During the first stage, the average grain size remains basically unchanged, and the hardness maintains at a value of ~20.18±0.26 GPa, despite the β-$Si_3N_4$ phase fraction increases from 7.67 to 57.34 wt%. Subsequently, the equiaxed grains transform into rod-like grains with a high aspect ratio via the reprecipitation process, resulting in a significant increase in the fracture toughness from 3.36±0.62 to 7.11±0.15 MPa·m$^{1/2}$. In the second stage of sintering process, the fraction of β-$Si_3N_4$ phase increases to 100.00 wt%, and the grain growth also rapidly occurs. Thus, the fracture toughness increases slightly to 7.61±0.42 MPa·m$^{1/2}$, but the hardness reduces to 16.80± 0.20 GPa. The current results demonstrate that the phase contents of β-$Si_3N_4$ and the microstructure shall be carefully tailored to achieve high-performance $Si_3N_4$ ceramics. $Si_3N_4$ ceramics with a fine-grained bimodal microstructure, consisting of the main α- and β-phases, can exhibit the optimized combination of hardness and toughness.

**Keywords:** silicon nitride ($Si_3N_4$); phase composition; microstructure; hardness; toughness

## 1 Introduction

Silicon nitride ($Si_3N_4$) ceramics have been considered and designed for a variety of structural applications, such as automotive engine parts, heat exchangers, pump seal parts, ball bearings, cutting tools, high resistance to thermal shock, tribological wear and chemical corrosion, excellent fatigue and creep resistance due to its low bulk density, unique microstructure characteristics, and excellent mechanical properties at ambient and high temperatures [1–5]. The polytypes of $Si_3N_4$-based ceramics mainly include α- and β-$Si_3N_4$ phases, and the microstructure often consists of equiaxed and bimodal grained microstructures. Generally, $Si_3N_4$ ceramics with high hardness (> 18 GPa) but low toughness (< 5 MPa·m$^{1/2}$) exhibit a major α-phase and a fine equiaxed microstructure [6,7]. On the other hand, the tough $Si_3N_4$ ceramics (> 5 MPa·m$^{1/2}$) are composed

* Corresponding authors.
E-mail: W.-M. Guo, guo1238@126.com;
H.-T. Lin, huataylin@comcast.net

of the major elongated β-phase grains and the coarsened bimodal microstructure, but it is usually with the low hardness (< 18 GPa) [8,9].

The mechanical properties of $Si_3N_4$ ceramics, in general, are mainly governed by the ratio of α/β phase content and morphology, including grain size, aspect ratio, and grain boundary phase composition and microstructure [10–12]. In order to improve the mechanical properties of $Si_3N_4$ ceramics, many researches have been carried out to control the α/β phase ratio and microstructure. For example, $Si_3N_4$ ceramics with both high fracture toughness and strength could be obtained by tailoring the β/(α+β) phase ratio of ~60–80 wt% [9,10]. Furthermore, self-reinforced $Si_3N_4$ ceramics with high fracture toughness and high bending flexural strength could be obtained by adding β-seed crystals, whose process involved tailoring the size and amount of well-dispersed elongated grains in a fine-grained matrix [13–15]. However, it would often inversely result in the relatively low Vickers hardness [16]. So far, it is not yet fully understood that what kind of combination of α/β phase proportion and microstructure can lead to both high hardness and high toughness of $Si_3N_4$ ceramics.

Herein, $Si_3N_4$ ceramics with different phase compositions and microstructures were prepared by spark plasma sintering (SPS) at different temperatures ranging from 1500 to 1800 ℃. The proportions of α/β phase and microstructure were systematically quantified as well. This study aimed to clarify what the phase composition and microstructure in terms of quantified values could produce $Si_3N_4$ ceramics with excellent mechanical properties of high hardness and high toughness.

## 2 Experimental

Commercial α-$Si_3N_4$ powders (purity > 95 wt%, particle size: 0.3 μm; UBE Industries, Ltd., Japan) were used as the raw material to mix with MgO (purity: 99.9%, particle size: 100 nm; Hangzhou Wanjing New Material Co., Ltd., China) and $Yb_2O_3$ sintering additives (purity: 99.995%, particle size: 3–6 μm; Beijing Founde Star Science and Technology Co., Ltd., China). The sample powders were prepared according to the volume fraction of $Si_3N_4$ : MgO : $Yb_2O_3$ = 95 : 3 : 2. The raw materials were mixed with $Si_3N_4$ milling balls in anhydrous ethanol for 24 h by using a planetary mill (QXQM-4L, Changsha Tianchuang Powder Technology Co., Ltd., China), and the slurry was subsequently dried in rotary evaporation and sieved through a 150-μm mesh to minimize agglomeration. The dried mixtures were consolidated by an SPS instrument (H-HPD-10-FL, FCT Systeme GmbH, Germany), using a graphite die with an inner diameter of 20 mm. The samples were sintered at different temperatures of 1500, 1600, 1650, 1700, and 1800 ℃ for 10 min in an Ar atmosphere. The heating rate was 100 ℃·min$^{-1}$, and the uniaxial pressure of 30 MPa was applied at temperatures above 1200 ℃. The samples prepared in this study were then labeled as SN1500, SN1600, SN1650, SN1700, and SN1800, as listed in Table 1.

The bulk densities of the sintered samples were measured by using the Archimedes method in distilled water. Based on the rule of mixtures, the relative density was determined by the ratio of bulk density to theoretical density. The qualitative and quantitative phase analyses of the SPSed specimens were carried out by the X-ray diffractometer (D8 ADVANCE, Bruker Corp., Germany). The mass fraction of β-$Si_3N_4$ ($\omega(\beta)$) was calculated by a direct comparison method [17]. The intensities ($I$) of the two highest peaks for both α-$Si_3N_4$ and β-$Si_3N_4$ phases were measured from the X-ray diffraction (XRD) patterns. For the β-$Si_3N_4$ phase, peaks at 27.1° and 36.1° were selected, which corresponded to the (200) plane and (120) plane, respectively; for α-$Si_3N_4$ phase, peaks at 31.0° and 35.4° were selected, which corresponded to the (201) plane and (210) plane, respectively. $\omega(\beta)$ was calculated as $\omega(\beta) = (I_{\beta(200)} + I_{\beta(120)})/(I_{\alpha(210)} + I_{\alpha(201)} + I_{\beta(200)} + I_{\beta(120)}) \times 100\%$, while that of α-$Si_3N_4$ phase ($\omega(\alpha)$) was then calculated as $\omega(\alpha) = 100\% - \omega(\beta)$ [18].

The microstructures of the SPSed samples were examined by using the scanning electron microscope (SEM; LYRA-3-XMU, TESCAN, Czech Republic). Before the SEM analysis of the sintered materials, the

**Table 1 Starting powder compositions, sintering temperatures, relative densities, and contents of β-$Si_3N_4$ phase of the sintered $Si_3N_4$ ceramics**

| Label | Starting powder composition (vol%) | Sintering temperature (℃) | Relative density (%) | $\omega(\beta)$ (%) |
|---|---|---|---|---|
| SN1500 | 95$Si_3N_4$–3MgO–2$Yb_2O_3$ | 1500 | 98.96 | 7.67 |
| SN1600 | 95$Si_3N_4$–3MgO–2$Yb_2O_3$ | 1600 | 99.01 | 41.42 |
| SN1650 | 95$Si_3N_4$–3MgO–2$Yb_2O_3$ | 1650 | 98.88 | 57.34 |
| SN1700 | 95$Si_3N_4$–3MgO–2$Yb_2O_3$ | 1700 | 98.83 | 87.70 |
| SN1800 | 95$Si_3N_4$–3MgO–2$Yb_2O_3$ | 1800 | 98.93 | 100.00 |

polished surfaces of all the samples (perpendicular to the pressing direction during SPS) were plasma etched for 120 s at a power of 300 W using $CF_4$ : $O_2$ mixed gas at a ratio of 90 : 10. The grain size, rod-like grain diameter, aspect ratio, rod crystal fraction, and the quantity of rods per unit area of $Si_3N_4$ grains in the materials were then determined by using ImageJ software. A statistically significant number of $Si_3N_4$ grains (~400–500 grains) were measured for each sample. It was worth noting that the quantity of rods per unit area was determined by the ratio of the quantity of rods to the total area in the SEM image.

The Vickers hardness of the materials was measured on the polished surfaces by the indentation method (HXD-2000TM, Shanghai Taiming Optical Instrument Co., Ltd., China) with an applied load of 4.9 N for 10 s. The Vickers indentation method (HVS-30Z, Shanghai Taiming Optical Instrument Co., Ltd., China) was applied to determine the fracture toughness with a loading force of 98 N and a holding pressure of 10 s. A higher load used in toughness measurement was essential to yielding crack propagation and a toughness value within the long crack region. The fracture toughness ($K_{IC}$) of the specific direction is measured by evaluating the crack length of the direction according to the equation proposed by Evans and Charles [19], and then calculated by Eq. (1):

$$K_{IC} = P\left[\pi\left(\frac{C_1 + C_2}{4}\right)\right]^{-\frac{3}{2}}\left(\tan\frac{\alpha}{2}\right)^{-1} \quad (1)$$

where $P$ is the indentation load (N), $C_1$ and $C_2$ are the measured diagonal crack lengths (m), and $\alpha$ (= 136°) is an angle of the diamond indenter.

## 3 Results

Figure 1 presents the XRD patterns of $Si_3N_4$ ceramics sintered at different temperatures. The results show that the phases in SN1500, SN1600, SN1650, and SN1700 are consisted of α-$Si_3N_4$ and β-$Si_3N_4$ phases. $\omega(\beta)$ for all samples are calculated and presented in Table 1. When the sintering temperature is 1500 ℃, α-$Si_3N_4$ is the main phase, and β-$Si_3N_4$ is the secondary phase. As the temperature increases to 1650 ℃, the $I$ of the β-$Si_3N_4$ increases, and the β-$Si_3N_4$ phase becomes as the major phase, whose content increases from 7.67 to 57.34 wt%. Only β-$Si_3N_4$ phase is detected, and the α-$Si_3N_4$ phase completely disappears when the temperature

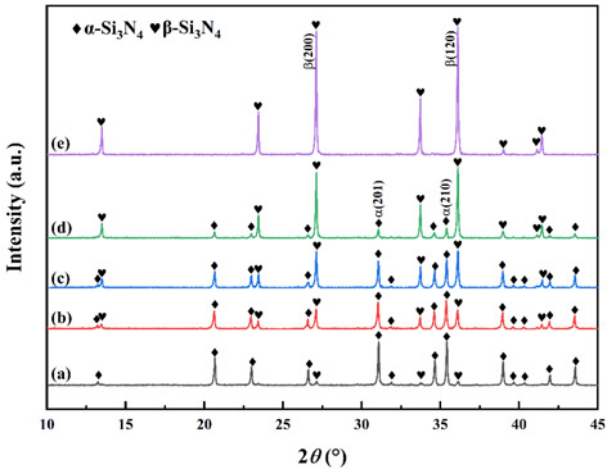


**Fig. 1** XRD patterns of $Si_3N_4$ ceramics: (a) SN1500, (b) SN1600, (c) SN1650, (d) SN1700, and (e) SN1800.

further increases to 1800 ℃, indicative of a complete phase transformation. During the sintering process, as the temperature increases, the sintering additives and the surface oxide of α-$Si_3N_4$ particles (i.e., $SiO_2$) form an oxynitride liquid phase [20], which promotes α- to β-$Si_3N_4$ phase transformation through the dissolution and reprecipitation mechanism.

Figure 2 shows the SEM images of plasma-etched surface of $Si_3N_4$ samples. The relative density values of all samples are calculated and presented in Table 1. The results of density measurements show that all of the relative density values are above 98%, which suggests that the nearly full densification has been achieved in all sintered samples. No apparent porosity is observed in all samples, suggesting that nearly full densification has been achieved, consistent with the relative density results. The SEM observations show that $Si_3N_4$ grains in SN1500 are mainly equiaxed shapes (Fig. 2(a)). A few needle-like grains are observed in SN1600 (Fig. 2(b)). A large fraction of the rod-like grains start to form in SN1650 (Fig. 2(c)), indicative of the formation of bimodal microstructures composed of both elongated and equiaxed grains. The $Si_3N_4$ grains become coarsened in SN1700 and SN1800 due to the higher sintering temperatures (Figs. 2(d) and 2(e)). Not only the fine equiaxed grains grow larger, but the diameter of elongated rod-like grains also becomes thicker due to Ostwald ripening. Therefore, the SPS technique can be applied to densify $Si_3N_4$ ceramics at relatively low temperatures, promoting the phase transformation and rod-like grain development [21–23], which well explains the fine-grained bimodal microstructure of SN1650 (Fig. 2(c)).

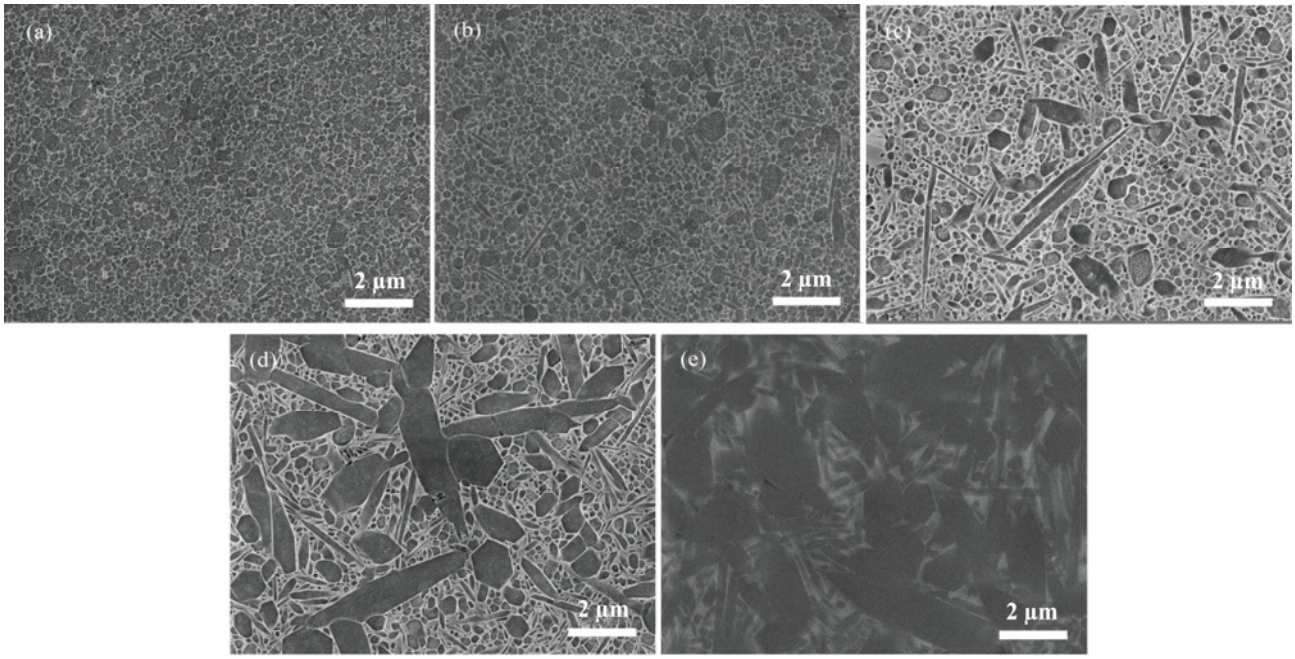


**Fig. 2** SEM images of plasma-etched surfaces of the SPSed $Si_3N_4$ ceramics: (a) SN1500, (b) SN1600, (c) SN1650, (d) SN1700, and (e) SN1800.

Figure 3 shows the mechanical properties of all of the SPSed $Si_3N_4$ ceramics. The Vickers hardness of SN1500, SN1600, SN1650, SN1700, and SN1800 is measured to be 21.49±0.48, 21.03±0.73, 20.18±0.26, 17.68±0.34, and 16.80±0.20 GPa, respectively. The results of hardness show a decreasing trend with the increase in sintering temperature, in particular for SN1700 and SN1800. In addition, the fracture toughness values of SN1500, SN1600, SN1650, SN1700, and SN1800 are measured to be 3.36±0.62, 4.60±0.16, 7.11±0.15, 7.57±0.76, and 7.61±0.42 MPa·m$^{1/2}$, respectively. As the sintering temperature increases from 1500 to 1650 ℃, the fracture toughness significantly increases from 3.36±0.62 to 7.11±0.15 MPa·m$^{1/2}$. Whereas, the toughness increases slightly from 7.11±0.15 to 7.61±0.42 MPa·m$^{1/2}$ when the temperature increases from 1650 to 1800 ℃.

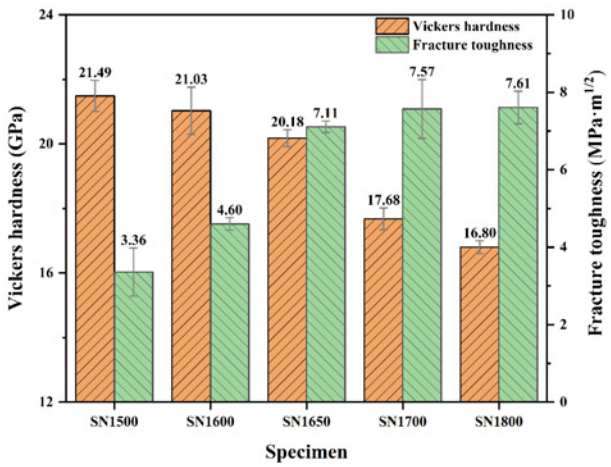


**Fig. 3** Vickers hardness and fracture toughness of the SPSed $Si_3N_4$ ceramis.

## 4 Discussion

### 4.1 Phase and microstructural development in two stages

It has been well recognized that the mechanical properties of $Si_3N_4$ ceramics are closely related to the quality of raw powder materials, oxide sintering additive, densification condition, phase content, and microstructure. In the present study, the raw powder materials and sintering additives employed are all identical. In addition, all samples are nearly fully densified under the sintering conditions employed in this study. Therefore, this study mainly focuses on the effects of phase composition and microstructure on the mechanical properties of $Si_3N_4$ ceramics.

Figure 4 shows the changes of phase composition and grain size developed under the sintering temperatures from 1500 to 1800 ℃. When the temperature arises from 1500 to 1650 ℃, the β-$Si_3N_4$ phase content increases from 7.67 to 57.34 wt%, while the grain size increases slightly. As the temperature increases from 1650 to 1800 ℃, the β-$Si_3N_4$ phase

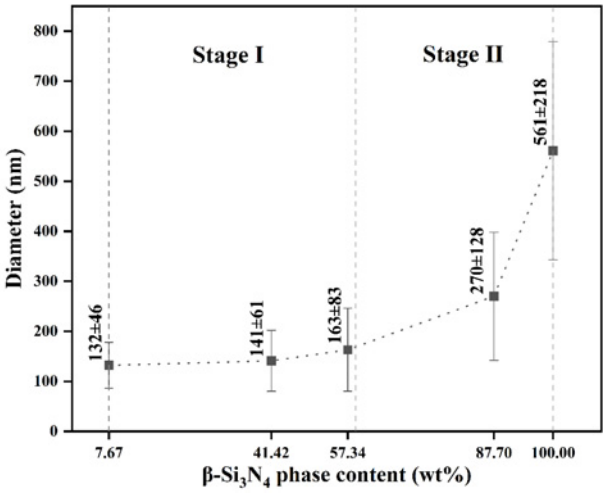


**Fig. 4** Average grain sizes of monolithic $Si_3N_4$ ceramics with different β-$Si_3N_4$ phase contents.

content increases from 57.34 to 100.00 wt%, accompanied by a significant increase in grain size. According to the results of the XRD patterns, the phase transformation begins at below 1600 ℃, and the α–β transformation in $Si_3N_4$ requires a lattice reconstruction. The α-$Si_3N_4$ dissolves in the liquid phase and reprecipitates as β-$Si_3N_4$, which in turn grows in the longitudinal direction as prismatic hexagonal rod-like crystals [24]. The grain growth along *c*-axis is dominant, but the growth along *a*-axis and *b*-axis can be negligible in the early stage of the α–β phase transformation [25]. Although the development of β-$Si_3N_4$ grains with high aspect ratios still takes place, the overall growth of grain size is not apparent at lower temperatures due to the low driving force.

Based on the variation trends of phase composition and grain size, two stages are featured in terms of phase composition and microstructure. First, the α–β phase transformation occurs with a fine-grained bimodal microstructure in Stage I, and the subsequent development including the coarsening of the rod-like grains with the β phase as the major phase becomes evident in Stage II. It can be concluded that the grain size growth in Stage I lags behind the phase transformation.

### 4. 2 Effect of phase composition and microstructural changes on mechanical properties in Stage I

The Vickers hardness of $Si_3N_4$ ceramics is mainly influenced by the α-$Si_3N_4$ phase content, the average grain size, porosity, and secondary grain boundary phase [26,27]. Since all samples are close to complete densification and prepared from the same raw powder materials, the effect of phase content and grain size on hardness will be primarily discussed in Sections 4.2 and 4.3. In general, α-$Si_3N_4$ exhibits higher hardness than β-$Si_3N_4$, and the ceramics with small matrix grain sizes exhibit high hardness. The results show that the grain size of $Si_3N_4$ grows slightly from 132±46 nm in SN1500 to 163±83 nm in SN1650, while the content of α-$Si_3N_4$ phase decreases from 92.33 to 42.66 wt%, resulting in a slight decrease in hardness from 21.49± 0.48 GPa in SN1500 to 20.18±0.26 GPa in SN1650. At this stage, the effect of grain growth on the hardness can be assumed to be negligible, so the reduction of the hardness in Stage I can be mainly attributed to the decrease of the fraction of α-$Si_3N_4$ phase.

The fracture toughness of $Si_3N_4$ ceramics depends mainly on the shape and size of grains and the composition of the grain boundary phases [27]. The dominant toughening mechanisms are governed by the grain diameter, aspect ratio, amount, and volume fraction of elongated grains [28–31]. The quantities, volume fractions, and aspect ratios of the elongated β-$Si_3N_4$ grains from the SEM observation are counted to statistically evaluate the effects of the elongated-grain microstructure on the toughness, as shown in Figs. 5 and 6. At the same time, in order to reveal the crack toughening mechanism, the SEM images of crack propagation paths are also provided in Fig. 7.

There are very few elongated grains formed in SN1500, and thus the operative mechanisms of toughening in $Si_3N_4$, such as crack deflection, crack bridging, and rod-like grain pull-out, are not observed (Fig. 7(a)), resulting in the lowest fracture

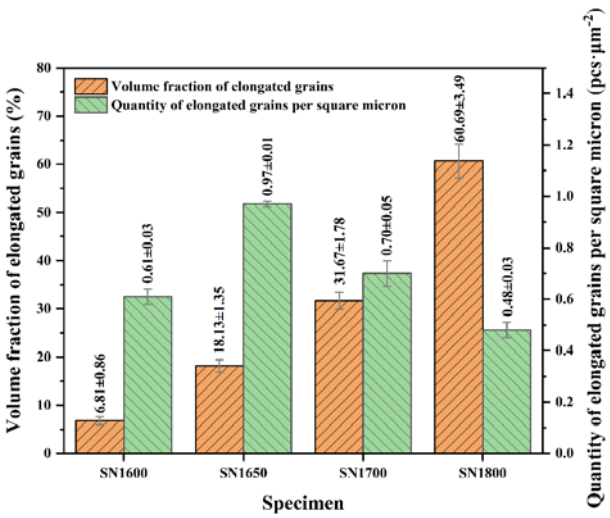


**Fig. 5** Volume fractions of the elongated grains and quantities of elongated grains per square micron in the SPSed $Si_3N_4$ ceramics.

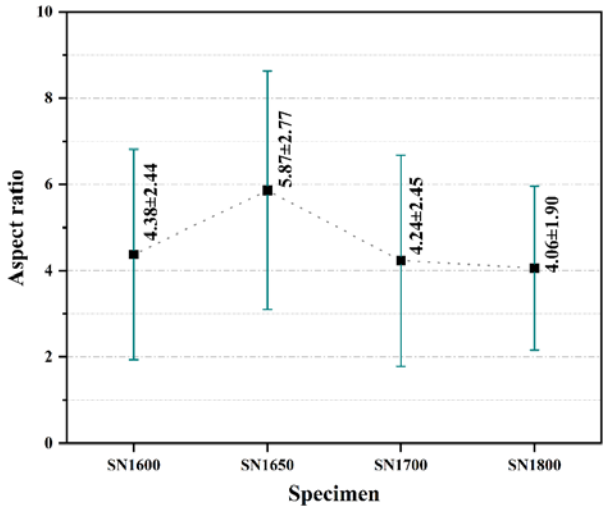


**Fig. 6** Aspect ratios of the elongated grains in monolithic $Si_3N_4$ ceramics sintered at different temperatures.

toughness (3.36±0.62 MPa·m$^{1/2}$). The quantitative analyses show that the volume fractions of elongated grains increase from 6.81%±0.86% in SN1600 to 18.13%±1.35% in SN1650, and the quantities of elongated grains per square micron elevate from 0.61±0.03 to 0.97±0.01 pcs·μm$^{-2}$, which promote the contributions of those operative toughening mechanisms. Meanwhile, elongated β-$Si_3N_4$ grains grow much faster along the [001] direction than along the [210] direction during the phase transformation [32,33], resulting in a pronounced increase in the aspect ratio from 4.38±2.44 in SN1600 to 5.87±2.77 in SN1650. The $Si_3N_4$ ceramics with a higher fraction of the elongated rod-like crystals is then expected to exhibit a better resistance to crack propagation [20]. As a consequence, the obvious features of crack deflection and crack bridging are observed in SN1650 (Fig. 7(c)) so that SN1650 exhibits the relatively high toughness (7.11± 0.15 MPa·m$^{1/2}$).

### 4. 3 Effect of phase composition and microstructural changes on mechanical properties in Stage II

The grain size of $Si_3N_4$ ceramics increases significantly from 163±83 nm in SN1650 to 561±218 nm in SN1800, and α-$Si_3N_4$ phase completely transforms to β-$Si_3N_4$ phase in SN1800, resulting in an apparent decrease in hardness from 20.18±0.26 to 16.80±0.20 GPa. It can be assumed that the small reduction in hardness in Stage I (from 21.49±0.48 to 20.18±0.26 GPa) is mainly due to the α–β phase transformation. The hardness of $Si_3N_4$ ceramics with a high α-$Si_3N_4$ content (19–22 GPa) is higher than that of pure β-$Si_3N_4$ (14–18 GPa) [34]. Whereas, the combined effect of phase transformation and grain growth results in a significant reduction in hardness but a slight increase in toughness in Stage II.

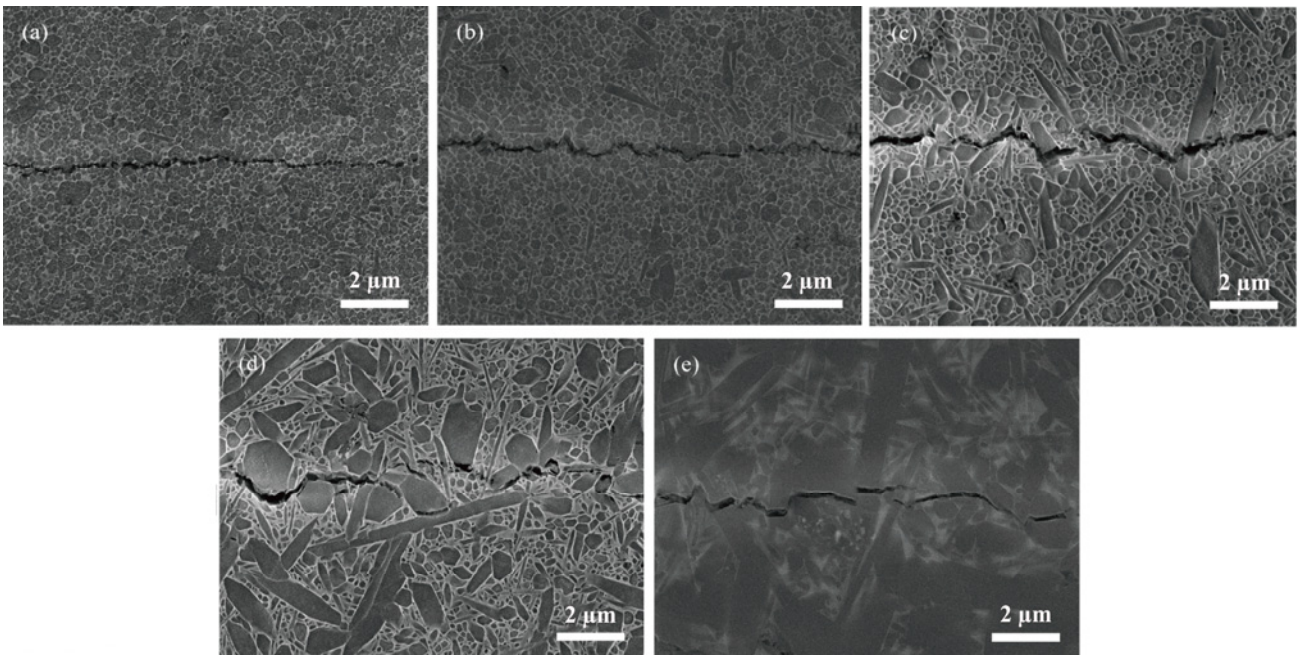


**Fig. 7** SEM images of crack propagation paths in $Si_3N_4$ ceramics: (a) SN1500, (b) SN1600, (c) SN1650, (d) SN1700, and (e) SN1800.

When the sintering temperature increases to 1800 ℃, as compared with that of SN1650, the phase transformation process has been completed, and the content of β-$Si_3N_4$ phase increases by about 43 wt%. The volume fractions of elongated grains of SN1800 increase markedly from 18.13%±1.35% in SN1650 to 60.69%±3.49%. However, the aspect ratios of elongated grains decrease from 5.87±2.77 in SN1650 to 4.06±1.90 in SN1800, and the quantities of elongated grains per square micron decrease from 0.97±0.01 to 0.48±0.03 pcs·μm$^{-2}$. On the other hand, the XRD results show that the phase transformation is completed between 1700 and 1800 ℃. Previous studies [25,35] showed that the reduction of the aspect ratio after the α–β phase transformation was a consequence of anisotropic Ostwald ripening. The increase in volume fractions of elongated grains of SN1800 is mainly due to the coarsening of elongated grains. The decrease of aspect ratio and quantity of elongated grains per square micron can lead to a slight increase in toughness from 7.11±0.15 MPa·m$^{1/2}$ in SN1650 to 7.61±0.42 MPa·m$^{1/2}$ in SN1800.

### 4.4 Phase composition–microstructure–mechanical properties

Based on the above discussion, the parameters for the phase fraction and microstructure features are summarized in Table 2 for assessing simultaneously high hardness and toughness. A schematic diagram of the mechanical properties of $Si_3N_4$ ceramics controlled by phase composition and microstructure is presented in Fig. 8.

As evidenced in SN1500 in Table 2, $Si_3N_4$ ceramics with the α phase as the dominant phase and a fine-grained equiaxed microstructure will exhibit high hardness but low fracture toughness (Fig. 8(a)). When the grain growth lags behind the phase transformation, a fine-grained bimodal microscopic morphology will be formed, which is confirmed by the aspect ratio and quantity of elongated grains in SN1650. At the expense of a slight decrease in hardness, the fracture toughness can be greatly improved, and therefore, $Si_3N_4$ ceramics with both high hardness and high toughness can be obtained (Fig. 8(b)). As the grain growth and phase transformation continue, the delay between phase formation and microstructural development disappears, leading to a microscopic morphology of coarse β-$Si_3N_4$ grains. In this case, the improvement of toughness is limited, and the hardness will also be substantially reduced, resulting in $Si_3N_4$ ceramics with high toughness and low hardness (Fig. 8(c)). Therefore, to obtain $Si_3N_4$ ceramics with high hardness and high toughness, the microstructural design is thus mainly governed by the phase content, average grain size,

**Table 2 Comparison of the phase fraction and microstructure features among the three samples in this work**

| Sample | SN1500 | SN1650 | SN1800 |
|---|---|---|---|
| α-$Si_3N_4$ : β-$Si_3N_4$ ratio | 92.33 : 7.67 | 42.66 : 57.34 | 0 : 100.00 |
| Average grain size (nm) | 132±46 | 163±83 | 561±218 |
| Aspect ratio | — | 5.87±2.77 | 4.06±1.90 |
| Quantity of elongated grains (pcs·μm$^{-2}$) | — | 0.97±0.01 | 0.48±0.03 |
| Vickers hardness (GPa) | 21.49±0.48 | 20.18±0.26 | 16.80±0.20 |
| Fracture toughness (MPa·m$^{1/2}$) | 3.36±0.62 | 7.11±0.15 | 7.61±0.42 |

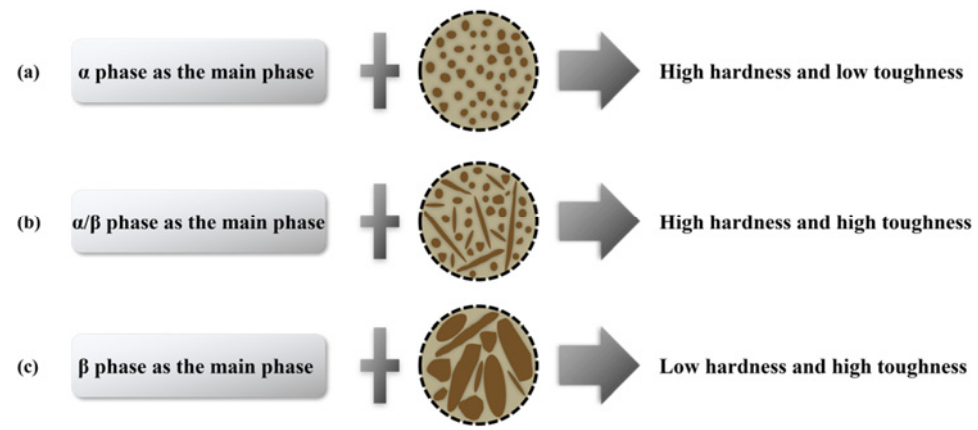


**Fig. 8** Schematic diagram of mechanical properties of $Si_3N_4$ ceramics controlled by phase composition and microstructure.

aspect ratio, and quantity of elongated grains per square micron. In this work, $Si_3N_4$ ceramics with a fine-grained bimodal microstructure consisting of the main α- and β-phases demonstrate the optimized combination of hardness and toughness.

In this study, the lag phenomenon is employed to obtain $Si_3N_4$ ceramics with high hardness and toughness. Due to the contribution of rod-like grains to fracture toughness, the phase proportion and microstructure shall be quantitatively assessed and analyzed; in the latter of which, the aspect ratio and quantity of elongated grains can be used to evaluate the development process of rod-like grains. It is critical to forming a fine-grained bimodal microstructure to maintain both hardness and toughness. Otherwise, the diverge can lead to the combination of either high hardness/low toughness or high toughness/low hardness. Combined with the design of phase composition and microstructure, $Si_3N_4$ ceramics with both high hardness and high toughness can be successfully achieved, which is of importance for future engineering design strategies, especially for cutting tool applications. When using $Si_3N_4$ ceramics as cutting tools to machine cast iron, the longer tool life is attributed to the high hardness and better abrasive wear resistance. Simultaneously, high toughness is also required to prevent tool chipping during high-speed cutting [36]. Ultimately, $Si_3N_4$ ceramics with high hardness and high toughness can have significant potential for applications in cutting tool industry.

## 5 Conclusions

The present study investigated the relationship between the phase composition, microstructure, and mechanical properties of $Si_3N_4$ ceramics prepared by SPS at temperatures ranging from 1500 to 1800 ℃. According to the phenomenon that grain growth lags behind the phase transformation process to a large extent, two stages with different phase and microstructure features are thus proposed. In Stage I, although the β-$Si_3N_4$ phase fraction increases from 7.67 to 57.34 wt%, the average grain size grows slightly from 132±46 to 163±83 nm. As a consequence, the hardness remains at the level of ~20.18±0.26 GPa, accompanied by the transformation of equiaxed grains to rod-like grains with high aspect ratios, leading to a significant increase in fracture toughness from 3.36±0.62 to 7.11±0.15 MPa·$m^{1/2}$. In Stage II, the content of β-$Si_3N_4$ phase increases to 100.00 wt%, accompanied by grain coarsening, resulting in a slight increase in fracture toughness to 7.61±0.42 MPa·$m^{1/2}$ but a decrease in hardness to 16.80±0.20 GPa. By careful engineering design of the phase composition and microstructure of $Si_3N_4$ ceramics, high-hardness and high-toughness $Si_3N_4$ ceramics (hardness ≈ 20.18±0.26 GPa, toughness ≈ 7.11±0.15 MPa·$m^{1/2}$) can be successfully obtained, whose phase composition and microstructure can probably be defined as α-$Si_3N_4$ : β-$Si_3N_4$ ratio = 42.66 : 57.34, average grain size = 163±83 nm, aspect ratio = 5.87±2.77, and quantity of elongated grains per square micron = 0.97±0.01 pcs·$\mu m^{-2}$. The present study suggests that the full understanding of the relationship between phase transformation and grain growth mechanism will enable the fabrication of desired high-performance $Si_3N_4$ ceramics achieved by precisely designing the phase composition and microstructure.

### Acknowledgements

This work was supported by the Shandong Provincial Key Research and Development Program (2019JZZY010330), the National Natural Science Foundation of China (52172066 and 52172064), the Key Research and Development Project of Gansu Province (21YF5WA140), and the Science and Technology Program of Guangzhou (201704030095). Shi-Kuan Sun acknowledges the Guangdong Key Platform & Programs of the Education Department of Guangdong Province (2021ZDZX1003) and the Opening Project of State Key Laboratory of High Performance Ceramics and Superfine Microstructure (SKL202104SIC).

### Declaration of competing interest

The authors have no competing interests to declare that are relevant to the content of this article.

### References

[1] Zhu XW, Sakka Y. Textured silicon nitride: Processing and anisotropic properties. *Sci Technol Adv Mater* 2008, **9**: 033001.

[2] Qin XW, Li S, Zhao L, *et al*. Silicon nitride ceramics consolidated by oscillatory pressure sintering. *Ceram Int* 2020, **46**: 14235–14240.

[3] Hou YB, Li B, Shao CW, *et al*. Effect of high-temperature annealing in air and $N_2$ atmosphere on the mechanical properties of $Si_3N_4$ fibers. *Mater Sci Eng A* 2018, **724**: 502–508.

[4] Xu SS, Zhou XN, Zhi Q, *et al*. Anisotropic, biomorphic cellular $Si_3N_4$ ceramics with directional well-aligned nanowhisker arrays based on wood-mimetic architectures. *J Adv Ceram* 2022, **11**: 656–664.

[5] Dang XL, Zhao DL, Guo T, *et al*. Oxidation behaviors of carbon fiber reinforced multilayer SiC–$Si_3N_4$ matrix composites. *J Adv Ceram* 2022, **11**: 354–364.

[6] Petzow G, Herrmann M. Silicon nitride ceramics. In: *High Performance Non-oxide Ceramics II. Structure and Bonding*. Jansen M, Ed. Berlin: Springer Berlin Heidelberg, 2002, **102**: 47–167.

[7] Greskovich C, Gazza GE. Hardness of dense α- and β-$Si_3N_4$ ceramics. *J Mater Sci Lett* 1985, **4**: 195–196.

[8] Ziegler G, Heinrich J, Wötting G. Relationships between processing, microstructure and properties of dense and reaction-bonded silicon nitride. *J Mater Sci* 1987, **22**: 3041–3086.

[9] Kawaoka H, Adachi T, Sekino T, *et al*. Effect of α/β phase ratio on microstructure and mechanical properties of silicon nitride ceramics. *J Mater Res* 2001, **16**: 2264–2270.

[10] Kong JH, Ma HJ, Jung WK, *et al*. Self-reinforced and high-thermal conductivity silicon nitride by tailoring α–β phase ratio with pressureless multi-step sintering. *Ceram Int* 2021, **47**: 13057–13064.

[11] Ziegler A, McNaney JM, Hoffmann MJ, *et al*. On the effect of local grain-boundary chemistry on the macroscopic mechanical properties of a high-purity $Y_2O_3$–$Al_2O_3$-containing silicon nitride ceramic: Role of oxygen. *J Am Ceram Soc* 2005, **88**: 1900–1908.

[12] Lee CJ, Chae JI, Kim DJ. Effect of β-$Si_3N_4$ starting powder size on elongated grain growth in β-$Si_3N_4$ ceramics. *J Eur Ceram Soc* 2000, **20**: 2667–2671.

[13] Hirao K, Nagaoka T, Brito ME, *et al*. Microstructure control of silicon nitride by seeding with rodlike β-silicon nitride particles. *J Am Ceram Soc* 1994, **77**: 1857–1862.

[14] Dai JH, Li JB, Chen YJ, *et al*. Effect of the residual phases in β-$Si_3N_4$ seed on the mechanical properties of self-reinforced $Si_3N_4$ ceramics. *J Eur Ceram Soc* 2003, **23**: 1543–1547.

[15] De Pablos A, Osendi MI, Miranzo P. Correlation between microstructure and toughness of hot pressed $Si_3N_4$ ceramics seeded with β-$Si_3N_4$ particles. *Ceram Int* 2003, **29**: 757–764.

[16] Hyuga H, Jones MI, Hirao K, *et al*. Influence of rare-earth additives on wear properties of hot-pressed silicon nitride ceramics under dry sliding conditions. *J Am Ceram Soc* 2004, **87**: 1683–1686.

[17] Pigeon RG, Varma A. Quantitative phase analysis of $Si_3N_4$ by X-ray diffraction. *J Mater Sci Lett* 1992, **11**: 1370–1372.

[18] Fu L, Engqvist H, Xia W. Spark plasma sintering of biodegradable $Si_3N_4$ bioceramic with Sr, Mg and Si as sintering additives for spinal fusion. *J Eur Ceram Soc* 2018, **38**: 2110–2119.

[19] Evans AG, Charles EA. Fracture toughness determinations by indentation. *J Am Ceram Soc* 1976, **59**: 371–372.

[20] Hampshire S, Pomeroy MJ. Grain boundary glasses in silicon nitride: A review of chemistry, properties and crystallisation. *J Eur Ceram Soc* 2012, **32**: 1925–1932.

[21] Nishimura T, Mitomo M, Hirotsuru H, *et al*. Fabrication of silicon nitride nano-ceramics by spark plasma sintering. *J Mater Sci Lett* 1995, **14**: 1046–1047.

[22] Suganuma M, Kitagawa Y, Wada S, *et al*. Pulsed electric current sintering of silicon nitride. *J Am Ceram Soc* 2003, **86**: 387–394.

[23] Belmonte M, González-Julián J, Miranzo P, *et al*. Spark plasma sintering: A powerful tool to develop new silicon nitride-based materials. *J Eur Ceram Soc* 2010, **30**: 2937–2946.

[24] Hampshire S. Silicon nitride ceramics—Review of structure, processing and properties. *J Achiev Mater Manuf Eng* 2007, **24**: 43–50.

[25] Kitayama M, Hirao K, Toriyama M, *et al*. Modeling and simulation of grain growth in $Si_3N_4$—II. The α–β transformation. *Acta Mater* 1998, **46**: 6551–6557.

[26] Bahrami S, Zakeri M, Faeghinia A, *et al*. Effect of the alfa content on the mechanical properties of $Si_3N_4$/BAS composite by spark plasma sintering. *J Alloys Compd* 2018, **756**: 76–81.

[27] Tatarková M, Tatarko P, Šajgalík P. $Si_3N_4$ ceramics, structure and properties. In: *Encyclopedia of Materials: Technical Ceramics and Glasses*. Pomeroy M, Ed. Amsterdam, the Netherlands: Elsevier Amsterdam, 2021, **2**: 109–118.

[28] Tatarko P, Lojanová Š, Dusza J, *et al*. Influence of various rare-earth oxide additives on microstructure and mechanical properties of silicon nitride based nanocomposites. *Mater Sci Eng A* 2010, **527**: 4771–4778.

[29] Šajgalík P, Dusza J, Hoffmann MJ. Relationship between microstructure, toughening mechanisms, and fracture toughness of reinforced silicon nitride ceramics. *J Am Ceram Soc* 1995, **78**: 2619–2624.

[30] Satet RL, Hoffmann MJ, Cannon RM. Experimental evidence of the impact of rare-earth elements on particle growth and mechanical behaviour of silicon nitride. *Mater Sci Eng A* 2006, **422**: 66–76.

[31] Šajgalík P, Galusek D. α/β Phase transformation of silicon nitride: Homogeneous and heterogeneous nucleation. *J Mater Sci Lett* 1993, **12**: 1937–1939.

[32] Krämer M, Wittmüss D, Küppers H, *et al*. Relations between crystal structure and growth morphology of β-$Si_3N_4$. *J Cryst Growth* 1994, **140**: 157–166.

[33] Lai KR, Tien TY. Kinetics of β-$Si_3N_4$ grain growth in $Si_3N_4$ ceramics sintered under high nitrogen pressure. *J Am Ceram Soc* 1993, **76**: 91–96.

[34] Peng GH, Li XG, Liang M, *et al*. Spark plasma sintered high hardness α/β $Si_3N_4$ composites with $MgSiN_2$ as additives. *Scr Mater* 2009, **61**: 347–350.

[35] Kitayama M, Hirao K, Toriyama M, *et al*. Modeling and simulation of grain growth in $Si_3N_4$—I. Anisotropic Ostwald ripening. *Acta Mater* 1998, **46**: 6541–6550.

[36] Tan DW, Zhu LL, Wei WX, *et al*. Performance improvement of $Si_3N_4$ ceramic cutting tools by tailoring of phase composition and microstructure. *Ceram Int* 2020, **46**: 26182–26189.